Biologically Inspired Optical-Flow Sensing for Altitude Control of Flapping-Wing Microrobots

*Pierre-Emile J. Duhamel, *Student Member, IEEE*, *Néstor O. Pérez-Arancibia, *Member, IEEE*,
Geoffrey L. Barrows, and Robert J. Wood, *Member, IEEE*

***Abstract*—We present the design and fabrication of a 33-mg 1-D optical-flow-based altitude sensor and its integration with a 68-mg flapping-wing flying microrobot. For the first time, an on-board sensor is successfully used to measure altitude for feedback control in a flyer of this size. Both the control strategy and the sensing system are biologically inspired. The control strategy relies on amplitude modulation mediated by optical-flow sensing. The research presented here is a key step toward achieving the goal of complete autonomy for at-scale flying robotic insects, since this demonstrates that strategies for controlling flapping-wing microrobots in vertical flight can rely on optical-flow-based on-board sensors. In order to demonstrate the efficacy of the proposed sensing system and suitability of the combined sensing and control strategies, six experimental cases are presented and discussed here.**

***Index Terms*—Bioinspired optical-flow sensing, feedback control, flapping-wing flight, microrobots.**

I. INTRODUCTION

BASED on the ideas introduced in [1] and [2], a strategy for altitude control of flapping-wing flying 60-mg microrobots of the kind in [3] was presented in [4]. Also in [4], compelling experimental evidence demonstrating the suitability of the proposed approach for altitude control was presented. In those cases, the controller design relies on the notion of wing-stroke amplitude modulation and the vertical position of the robot is measured using an external laser position sensor. In this paper, we present the first controlled vertical flight of a 101-mg flapping-wing microrobot, in which the vertical position fedback into the controller is estimated using a biologically inspired optical-flow-based on-board sensor, similar to the one in [5]. This is a key step toward achieving the goal of complete autonomy for at-scale flying robotic insects, since these experimental results unequivocally demonstrate that microrobots of the kind considered here are capable of carrying the extra weight of on-board sensors. More importantly, these results demonstrate that strategies for controlling microrobots in vertical flight can rely on optical-flow-based sensing systems.

It has been suggested that in natural insects, among all the sensory modalities involved in flight control, visual stimuli are the predominant signals used for controlling position and orientation, and for maintaining stability during flight (see [6] and references therein). Also, it is believed that in unidirectional flight, natural insects use optical flow, defined as motion of the visual field relative to the eyes, for navigation. Interestingly, it has been known since the 1970s that for most insects, flight has prompted the evolution of the amazing information processing capabilities that we observe in flying insects today [7]. From a robotics perspective, there is evidence that some of the ideas about how insects sense their environment and navigate through it can be applied to generate high-level rules of navigation for terrestrial and flying robotic systems [8].

Inspired by the notion of optical flow, since the late 1990s, visual motion sensors have been developed and applied to a variety of flying prototypes [5], [8]–[18]. For instance, in [17], a 10-g fixed-wing *micro air vehicle* (MAV) capable of regulating airspeed and avoiding lateral collisions was developed, based on a navigation strategy that combines optical-flow and gyroscopic information. Another example is the work presented in [8]. There, several navigational strategies based on optical flow employed by bees were described. The feasibility of applying those strategies to robotic systems was tested using unmanned helicopters. Using a 13.6-g flapping-wing MAV, the potential benefits and limitations of using optical flow on flapping-wing robotic systems were explored in [18]. There, it is argued that periodic oscillations produced by flapping introduce significant bias to the estimates obtained from the measured optical flow.

One of the main contributions presented in this paper is the integration of an optical-flow sensor (model Tam4, designed and fabricated by Centeye[1]) with a flapping-wing flying microrobot similar to the one in [3], the *RoboBee*.[2] Furthermore, using modern system identification techniques, a filter is trained for extracting real-time velocity and linear position information from the optical-flow measurement. This extracted information

---

Manuscript received November 9, 2011; revised May 4, 2012 and October 1, 2012; accepted October 9, 2012. Date of publication December 13, 2012; date of current version January 10, 2013. Recommended by Guest Editor M. Sitti. This work was supported in part by the National Science Foundation under Award CCF-0926148 and in part by the Wyss Institute for Biologically Inspired Engineering. The work of P.-E. J. Duhamel was supported by a Graduate Research Fellowship from the National Science Foundation. This paper was presented in part at the 2012 IEEE International Conference on Robotics and Automation, Saint Paul, MN, May 14–18, 2012.

*P.-E. J. Duhamel and N. O. Pérez-Arancibia contributed equally to this work.

P.-E. J. Duhamel, N. O. Pérez-Arancibia, and R. J. Wood are with the School of Engineering and Applied Sciences, Harvard University, Cambridge, MA 02138 USA, and also with the Wyss Institute for Biologically Inspired Engineering, Harvard University, Boston, MA 02115 USA (e-mail: pduhamel@fas.harvard.edu; nperez@seas.harvard.edu; rjwood@eecs.harvard.edu).

G. L. Barrows is with Centeye, Inc., Washington, DC 20008 USA (e-mail: geof@centeye.com).

Color versions of one or more of the figures in this paper are available online at http://ieeexplore.ieee.org.

Digital Object Identifier 10.1109/TMECH.2012.2225635

[1] http://www.centeye.com

[2] http://robobees.seas.harvard.edu

is used for controlling the altitude of the flapping-wing microrobot considered here. Total autonomy of *RoboBee*-like MAVs will be achieved by the integration of power, sensing, and computational hardware into the robot, which implies the fulfillment of strict mass and size constraints. To the best of our knowledge, this is the first empirical demonstration of optical-flow-based control in an at-scale biologically inspired microrobot.

The suitability of the proposed approach is demonstrated using six experimental cases. The first case shows hovering, in which the optical-flow signal is generated using a static textured background composed of horizontal white and black stripes. The second case shows trajectory following, in which the optical-flow signal is generated using the same static textured background used in the first case. The third case shows motion tracking, in which during the first 10 s of the experiment, the optical-flow signal is generated using a static textured background, and then, the reference signal is fixed while the textured screen moves. Since the vertical position of the robot is estimated using optical flow, in order to compensate for the movement of the screen, the robot tracks it along the vertical axis. The fourth case shows motion tracking with zero reference, in which the robot takes off, hovers, tracks a trajectory, and lands entirely by following the motion of a patterned screen composed of horizontal white and black stripes. The fifth case shows hovering using a non-homogeneous natural-looking pattern. Finally, the sixth case shows trajectory following using the same non-homogeneous natural-looking pattern used in the fifth case.

The rest of this paper is organized as follows. Section II describes the flapping-wing microrobot used in the experiments and the main experimental setup. Section III describes the optical-flow sensor and the strategy for altitude control. Experimental results are presented in Section IV. Concluding remarks are given in Section V. The notation used in the paper is as follows. $\mathbb{R}$ and $\mathbb{Z}^+$ denote the sets of real and nonnegative integer numbers, respectively. The variable t is used to index discrete time, i.e., $t = \{kT_s\}_{k=0}^{\infty}$, with $k \in \mathbb{Z}^+$ and $T_s \in \mathbb{R}$, referred to as the sample-and-hold time. The variable τ is used to index continuous time, and therefore, for a generic continuous-time variable $x(\tau)$, $x(t)$ is the sampled version of $x(\tau)$. The expression z^{-1} denotes the delay operator, i.e., for a signal x, $z^{-1}x(k) = x(k-1)$, and conversely, $zx(k) = x(k+1)$. For convenience, z is also the complex variable associated with the z-transform.

II. DESCRIPTION OF THE MICROROBOT AND MAIN EXPERIMENTAL SETUP

A. *Microrobot and Lift Force Generation*

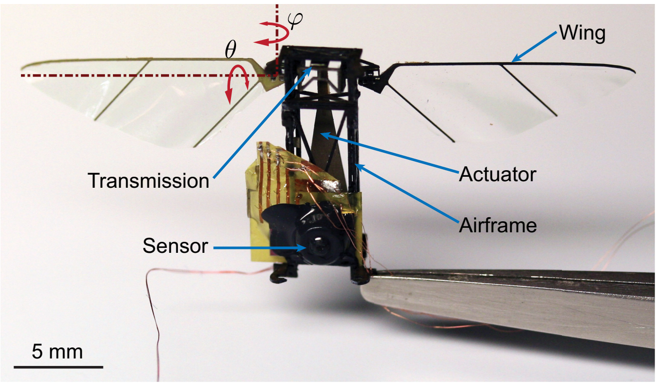

Fig. 1. Photograph of the biologically inspired microrobotic flying insect, the *RoboBee*, with the optical-flow-based altitude sensor integrated into its airframe. This prototype was entirely designed and fabricated by the authors at the Harvard Microrobotics Laboratory based upon designs which previously demonstrated the ability to liftoff [3]. The flapping angle is labeled by φ and the passive rotation is labeled by θ. The optical-flow sensor was assembled using flexible circuit fabrication techniques, as described in Section III.

The flapping-wing robotic insect developed for performing the experiments discussed in this paper is shown in Fig. 1. This prototype was entirely designed and fabricated at the Harvard Microrobotics Laboratory. The main flapping mechanism was developed based upon designs which previously demonstrated the ability to liftoff [3], but including new features that allow the mounting of the optical-flow-based sensor to be discussed in Section III. The main electromechanical components of the prototype include a piezoelectric bending bimorph cantilever actuator [19], a flexure-based transmission, a pair of airfoils, and an airframe which serves as a mechanical ground and as mounting point for the sensor. The transmission maps the approximately linear motions of the actuator into the flapping motion of the wings.

The robot generates forces through a phenomenon referred to as passive rotation [20], produced by connecting the robot's wings to the mechanical transmission through flexible hinges, which allow the wings to rotate according to the angle $\theta(\tau)$ in Fig. 1. This rotation is caused by the inertial forces produced by the flapping $\varphi(\tau)$ and by the aerodynamic forces generated by the interaction of the wings with the air. As explained in [20], an angle θ different than 0° implies that the wings have a positive angle of attack, which causes the generation of lift and drag forces acting on the wings' surfaces. The microrobot in Fig. 1 was designed such that, for sinusoidal actuator displacements, the magnitude of the drag force generated during the upstroke and the magnitude of the drag force generated during the downstroke are symmetric with respect to each other about the value 0, and the mean lift-force vector intersects the center of mass. Thus, ideally, no body torques are generated and the angles of rotation in three dimensions about the robot's center of mass (pitch, roll, and yaw) should stay at 0°.

In [4], following the ideas in [20]–[23] and references therein, it was argued that the mean total aerodynamic force Φ_T generated by a symmetrical pair of wings throughout a wing-stroke can be estimated by employing a quasi-steady blade-element method. This notion allows one to show that, assuming a sinusoidal stroke $\varphi(\tau) = \varphi_0 \sin(2\pi f_r \tau)$ and a horizontal stroke plane, regardless of the size and shape of the robot's wings, the estimated mean total flight force is directly dependent on f_r^2 and φ_0^2. This indicates that in order for flying insects to accelerate against gravity or hover at a desired altitude, they can modulate the average lift force by changing the stroke amplitude φ_0 or by changing the stroke frequency f_r. For the kind of robot considered here, the transmission that maps the actuator output, labeled as $\delta(t)$, to the stroke angle $\varphi(t)$ can be approximated by a constant κ_T, i.e., $\varphi(t) = \kappa_T \delta(t)$. Thus, by changing the amplitude and/or the frequency of $\delta(t)$, Φ_T can be modulated.

In steady state, the average discrete-time lift force can be estimated as

$$\Gamma_L(t) = \frac{1}{N_L} \sum_{i=0}^{N_L-1} \gamma_L(t - T_s i), \tag{1}$$

where $\gamma_L(t)$ is the sampled version of the continuous-time instantaneous lift force $\gamma_L(\tau)$. Here, $t = kT_s$, with a fixed $T_s \in \mathbb{R}$ and $0 < N_L \in \mathbb{Z}^+$. Note that assuming steady-state conditions, for the perfectly symmetric flapping case described in the previous paragraph, $\Gamma_L(t)$ can be thought of as an estimate of Φ_T.

From the previous paragraphs, it follows that the equation describing the robot's motion along the vertical axis is simply

$$\gamma_L(\tau) - mg - c\dot{x}(\tau) = m\ddot{x}(\tau), \tag{2}$$

where m is the mass of the robot, g is the gravitational acceleration constant, and $c\dot{x}$ is a term used to model the aerodynamical drag acting on the robot's body. As discussed in [1], [2], and [4], the instantaneous lift force $\gamma_L(\tau)$ is a nonlinear function of the frequency and amplitude of the flapping angle φ. Note that for sinusoidal inputs, instantaneous lift forces oscillate around some non-zero mean force, crossing zero periodically. Upward vertical movement occurs when the average lift force, estimated as in (1), overcomes the combined effects of mg and the body drag term $c\dot{x}$. Thus, control strategies for hovering and vertical trajectory following can rely on balancing the robot's weight by varying the amplitude of the flapping angle, according to a feedback law. In the experiments presented here, the signal fedback into the controller is optical flow.

B. Main Experimental Setup

An illustration of the optical-flow-based vertical flight control experiment is shown in Fig. 2. A photograph of the experimental setup is shown in Fig. 3. This setup is a modification of the one described in [4]. There, the vertical position of the microrobot is controlled employing a feedback law that uses a measurement of the altitude x for generating the control signal. In that case, x is measured using a long-range *charge-coupled device (CCD)* laser displacement sensor LK-2503 fabricated by Keyence. In the research presented here, the true altitude x is estimated employing a Tam4 on-board optical-flow sensor, designed and fabricated by Centeye. From this point onward, we assume that the signal measured with the external laser position sensor is noise free, and therefore, that this is the true altitude x. Consistently, the optical-flow-based estimate of x is labeled $\hat{x}$. The main topics discussed in this paper are the integration of the Tam4 sensor into the flying microrobot and the use of the optical-flow signal for estimating the robot's vertical position, used as feedback for real-time altitude control. The integration of the microrobot with the sensing system is shown in Fig. 1. The details about the sensor and the integration process are discussed in the next section.

Optical flow refers to the motion of the visual field relative to the eyes of the observer. The Tam4 sensor measures optical flow, and thus to increase the signal-to-noise ratio, in the first four experimental cases discussed here, a textured screen formed of parallel white and black stripes is placed in front of the sensor, as shown in Figs. 2 and 3. The textured screens are generated using a computer monitor. In this case, the robot's movement is constrained to the vertical degree of freedom using guide wires, and consequently, the optical-flow sensor moves in the vertical direction only. As seen in Fig. 2, the image signal captured by the Tam4 sensor is sent to a microprocessor (Arduino Mega 2560), in which a train of pulses, whose amplitudes are approximately

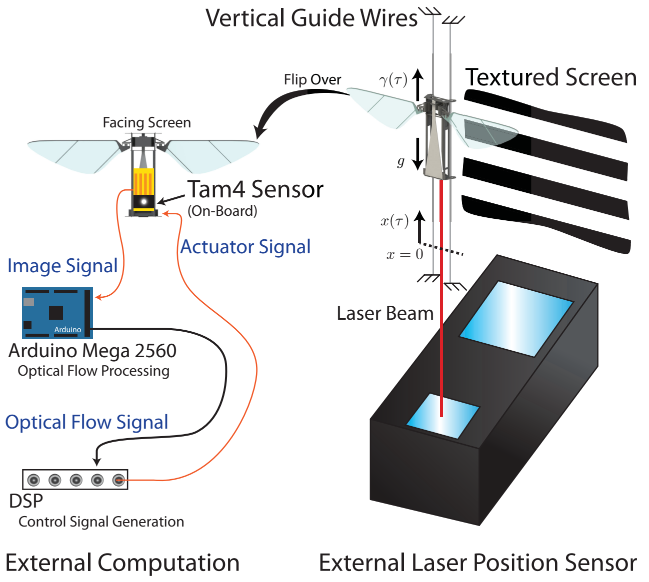

Fig. 2. Illustration of the setup used in the optical-flow-based altitude control experiments. The altitude x is estimated using an on-board Tam4 optical-flow sensor and a trained conversion filter. An external laser displacement sensor is used for training the filter that converts optical flow into altitude and for monitoring the position signal estimated by the conversion filter. The textured screen is generated using a commercial personal computer monitor.

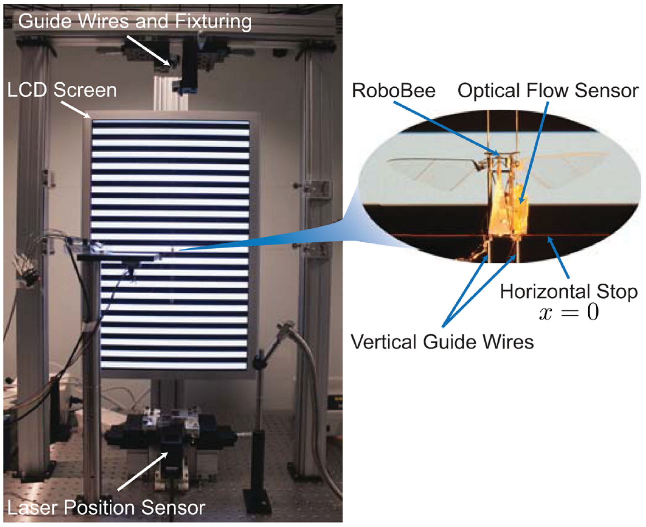

Fig. 3. Photograph of the experimental setup illustrated in Fig. 2, which is a modified version of the setup first presented in [4]. The screen patterns (textured and natural-looking) used in the optical-flow-based altitude control experiments are generated using a computer monitor. Note the relatively small size of the flapping-wing microrobot with respect to the entire setup.

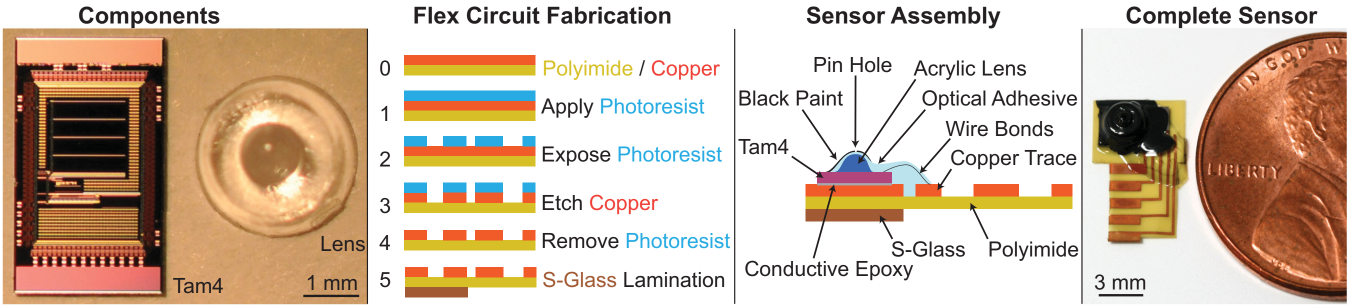

Fig. 4. Steps of sensor fabrication. *Components:* Tam4 bare die and acrylic injection-molded lens. The Tam4 chip is designed for 1-D motion sensing. In its displayed orientation, the Tam4 focal plane is 4 pixels high and 32 pixels wide and senses motion from left to right. *Flex Circuit Fabrication:* Beginning with a copper and polyimide substrate (0), a positive photoresist is applied to the copper surface (1). The photoresist is selectively removed by exposure to light (2) and the revealed copper is etched (3), such that, circuit traces are formed by the remaining copper protected by the unexposed photoresist. Finally, the photoresist is removed (4), and a patch of s-glass is laminated (5) to the polyimide surface behind the sensor for structural reinforcement. *Sensor Assembly:* Diagram of sensor assembly on the flex circuit substrate. First, the Tam4 chip is glued and wire-bonded to a flex circuit breakout. Then, the injection-molded lens is glued onto the Tam4 focal plane. Finally, an iris is painted onto the lens surface. *The Complete Sensor:* After the fabrication process is complete, the sensor's size is compared to a penny's size.

proportional to the vertical velocity of the microrobot, is generated. Then, the train of pulses, the optical-flow signal, is sent to a *digital signal processor* (DSP) in which, using an identified filter, the robot's position information is generated and the control signal input to the piezoelectric actuator is computed. Note that there is not a fundamental reason for using two processors, this is done for experimental convenience. For a final prototype, a single custom-designed processor would be necessary to meet the low mass and power consumption requirements for integration with the microrobot.

III. OPTICAL-FLOW SENSING AND ALTITUDE CONTROL

A. *Sensor Hardware and Integration With the Microrobot*

The Tam4 image sensor is custom-designed for low power and mass applications such as embedded systems and robotics. The sensor chip, shown on the first row of Fig. 4, consists of a 4×32 pixel array, optimized for sensing motion along a single axis. Pixels on the Tam4 have an $8:1$ aspect ratio with a pixel pitch of 336×42 μm, such that, the focal plane is a square with an area of 1.34 mm^2. The pixel electronics use a typical continuous-time logarithmic-response pixel circuit, allowing for a higher dynamic range of incident radiance to be captured within the output analog voltage range. The logarithmic response mode can also be operated without shuttering, which decreases the weight and complexity of the sensor assembly. The output pixel is selected using a 7-bit counter, with the first two upper bits selecting the row and the lower five bits selecting the column. By incrementing the value of the counter, the pixel array is scanned pixel-by-pixel row-wise, with the resulting pixel signal outputted as an analog voltage. The Tam4 has on-chip biases. This arrangement allows the chip to be operated with just five signals: ground, power, increment, reset, and output.

In order to create a complete camera, light is focused onto the chip's focal plane using an acrylic injection-molded lens, shown on the first row of Fig. 4. This lens is attached directly onto the Tam4 chip using UV curable optically clear adhesive. An iris is formed by covering the lens with black paint except for a hole at the top of the lens. The lens has a focal length just over 1 mm, resulting in a practical field of view of about 70°. When used in the experiments as shown in Figs. 2 and 3, the field of view includes approximately eight stripes of the textured screen used in the first four experiments presented in Section IV, which results in a sampling of approximately four pixels per stripe, completely adequate for the purposes of the control experiments discussed here. We further discuss this issue in Section IV.

When integrating the optical-flow sensor into the microrobot, as shown in Fig. 1, many factors are considered simultaneously, such that the resulting microrobotic system maintains its capability of lifting off and maneuvering along the vertical axis. All materials are chosen and components are made with low mass considerations. A flex circuit breakout, shown on the fourth row of Fig. 4, was designed to connect the bare die Tam4 with the off-board microcontroller used for processing optical flow, resulting in an interface that is significantly lighter than a typical fiberglass *printed circuit board* (PCB). The backing of the flex circuit was reinforced with s-glass around the Tam4 chip to add protection for the silicon chip and wire bonds with negligible added weight. The Tam4 bare die is glued with conductive epoxy to a ground pad on the flex circuit and necessary signals are wire bonded to 200-μm copper traces. Fine 51-AWG varnished copper wiring between the flex circuit and the optical-flow processor, used to transmit the image signal, adds minimal drag as the microrobot ascends along the vertical axis. The flex circuit fabrication process and assembly of the optical-flow sensor are shown on the second and third rows of Fig. 4, respectively.

The body design of the *RoboBee* in Fig. 1 is similar to the body design of the prototypes employed in the experiments presented in [4]. However, in this case, cross braces were added between the two lateral surfaces of the robot's structure, in order to support the mounting of the optical-flow sensor to the airframe. The final complete microrobotic device, as shown in Fig. 1, has the mass distribution shown in Fig. 5. The *sensor other* category, consisting of the flex circuit, solder, and glue, is currently the greatest mass contribution of the sensor components. The larger copper pads on the flex circuit breakout, as seen in Fig. 4, were primarily used for testing, and then, cut

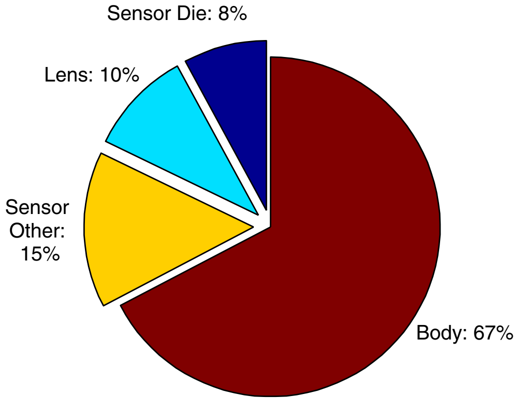

Fig. 5. Breakdown of the *RoboBee* (microrobot + on-board optical-flow sensor) mass by component. Total robot mass is 101 mg. *Sensor other* consists of flex circuit breakout, solder, and glue.

off in order to decrease the final mass of the prototype. There is still room for improvement in decreasing the weights of the various sensor components. For example, the lens mass could be decreased in a future iteration by using printed pinhole optics [24]. The fabrication method employed in the course of this research has allowed us to create an optical-flow-based altitude sensor that is significantly lighter than other current versions reported in the robotics literature. For example, one previous effort in miniaturization of optical-flow sensors, described in [25] and applied in [17], combined a 140-mg cut-down TSL3301 sensor fabricated by TAOS with 1×102 pixel resolution, a 170-mg lens with case, and a 80-mg PCB for a combined mass of 390 mg. Our 33-mg sensor offers high performance, as seen in Section IV, with approximately $\frac{1}{10}$ the mass of the sensor in [25] and [17], by using less packaging, lighter optics, and thinner circuitry.

As depicted in Fig. 2, the Tam4 image sensor interfaces with the off-board Arduino Mega 2560, which captures images and computes optical flow. The Arduino Mega 2560 is based on the ATmega2560, which is an 8-bit microcontroller, operating at 16 MHz with 256 KB of flash memory. Optical flow is computed using a modified version of the *Image Interpolation Algorithm* (IIA) [26], which requires minimal computational power and can be implemented with fixed point scaled integers. Since the Tam4 sensor is a 1-D sensor with a high aspect ratio array of pixels, optical flow is only calculated and communicated for the 1-D long axis of the image sensor. To further simplify the optical-flow calculations, only a single 1×32 pixel column from the captured images is used in the calculation of the 1-D optical-flow signal. The optical-flow signal is the input to the control algorithms that are computed by an off-board DSP, as illustrated in Fig. 2. The transmission of the resulting optical-flow signal is done using an RS-232 serial connection at 9600 Bd. The pulses composing the optical-flow train are received at a nonconstant rate of approximately 40.5 Hz. A buffering strategy in the communication between the two processors in Fig. 2 ensures that no data are lost in the transmission process.

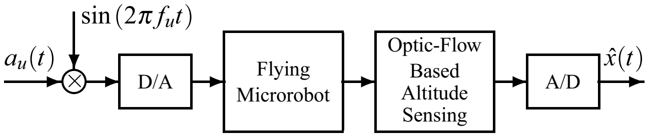

Fig. 6. Block diagram of the integrated microrobot with the proposed on-board sensing system, used in the altitude control experiments. Note that the true altitude $x(t)$ is estimated using an optical-flow-based sensing system. The resulting estimate is labeled as $\hat{x}(t)$.

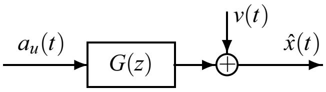

Fig. 7. Idealized system dynamics. $G(z)$: Discrete-time open-loop plant; $a_u(t)$: Amplitude of input $u(t)$; $\hat{x}(t)$: Estimated altitude; $v(t)$: Output disturbance, representing the aggregated effects of all the disturbances affecting the system, including stochastic wind currents. $G(z)$ is idealized under the assumption that the frequency f_u is fixed and that $a_u(t)$ oscillates around a_H, which is the exact amplitude required for hovering.

B. Control Strategy

In Section II, we explained that the average lift force $\Gamma_L(t)$ can be modulated by varying the frequency or amplitude of the sinusoidal flapping pattern $\varphi(\tau)$. As in [4], in the experiments presented here, we use amplitude modulation with a fix flapping frequency. Formally, the input signals to the piezoelectric actuator have the form

$$u(t) = a_u(t) \sin(2\pi f_u t) . \tag{3}$$

The idea is to think of $\sin(2\pi f_u t)$ as a part of the system, with f_u constant, as shown in Fig. 6, and consider $a_u(t)$ to be the control signal, generated according to some control law. This notion is illustrated in Fig. 7. Thus, in closed loop, we force the signal applied to the system in Fig. 7 to have the form

$$a_u(t) = \begin{cases} \overline{a_u} & \text{if } b_u(t) \geq \overline{a_u} \\ b_u(t) & \text{if } \underline{a_u} < b_u(t) < \overline{a_u} \\ \underline{a_u} & \text{if } b_u(t) \leq \underline{a_u}, \end{cases} \tag{4}$$

with

$$b_u(t) = K(z) e_x(t), \tag{5}$$

where $K(z)$ is a discrete-time *linear time-invariant* (LTI) operator depending on the delay operator z^{-1}. The real number $\underline{a_u} \in [0, 1]$ is the minimum allowable value that $a_u(t)$ can take (lower bound). The real number $\overline{a_u} \in [0, 1]$ is the maximum allowable value that $a_u(t)$ can take (upper bound). When using optical-flow for estimating altitude, the signal $e_x(t)$ is the control error defined as $e_x(t) = x_d(t) - \hat{x}(t)$, where $x_d(t)$ is the desired altitude and, as stated before, $\hat{x}(t)$ is the optical-flow-based estimated altitude signal, as depicted in Fig. 2. As proposed in [4], a model of the plant G in Fig. 7 can be found using modern system identification techniques. The system G is idealized under the assumption that the frequency f_u is fixed and that $a_u(t)$ oscillates around a_H, which is the exact amplitude required for hovering.

Note that in this case the system identification of G is extremely challenging from an experimental point of view, because

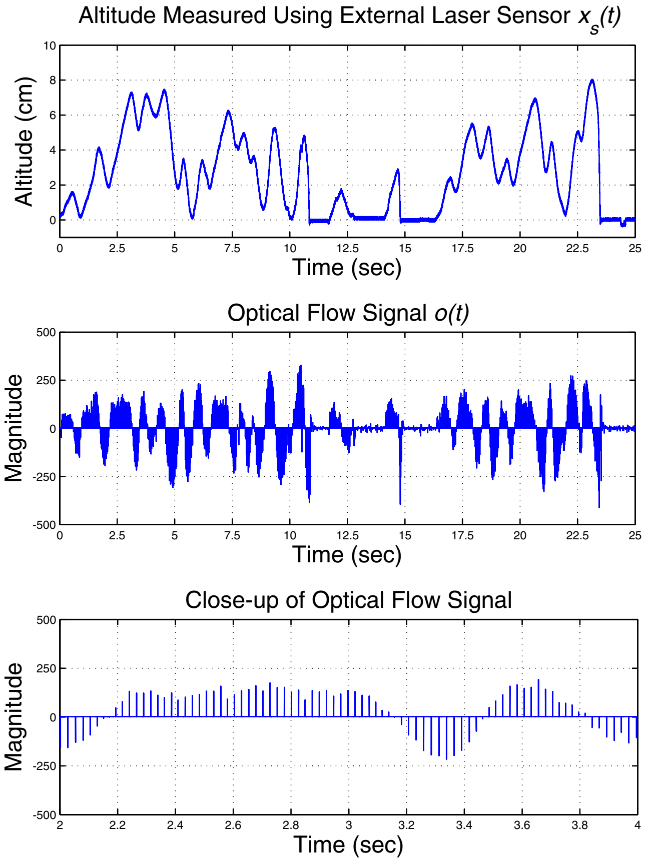

Fig. 8. Experimental data used for estimating the operator Ψ that maps the optical-flow signal, $o(t)$, to the estimated altitude, $\hat{x}(t)$, i.e., $\hat{x} = \Psi o$. *Upper Plot:* True altitude measured using external laser sensor, $x_s(t)$. *Middle Plot:* Optical-flow signal $o(t)$. *Bottom Plot:* Close-up of optical-flow signal $o(t)$.

the input–output data required for running the identification algorithm have to be obtained while the microrobot hovers around an equilibrium point. Here, using the experimental technique introduced in [4], a model of G, for the case $f_u = 110$ Hz, was computed. Using this identified model and classical controller design techniques, an LTI operator $K(z)$ for the law in (5) was found and evaluated, employing the classical gain and phase margin indices. For further details, see [4].

IV. EXPERIMENTAL RESULTS

A. *Conversion of Optical Flow to Altitude*

First in this subsection, we discuss the conversion from optical flow to altitude. The objective here is to find a dynamic mapping Ψ, from the optical-flow signal $o(t)$ to the estimated altitude $\hat{x}(t)$. In order to perform this estimation process, we use measurements of the robot's altitude obtained with the external long-range laser displacement sensor depicted in Fig. 2 and shown in Fig. 3. It is assumed that the measurement obtained with the laser displacement sensor is the *true* altitude $x(t)$. However, to emphasize the fact that a sensor is employed, in this subsection, we label this variable $x_s(t)$, i.e., $x(t) = x_s(t)$. The signal $\hat{x}(t)$ results from processing the optical-flow signal $o(t)$. Note that for convenience $o(t)$ is treated as a 10-KHz signal formed by zeros and spikes that contain the optical-flow information. In the upper plot of Fig. 8, a sequence of the altitude $x_s(t)$, sampled at 10 KHz, is shown. The middle plot in Fig. 8 shows the corresponding optical-flow train of pulses, spaced at a nonconstant frequency about 40.5 Hz, whose magnitude is approximately proportional to velocity. The bottom plot in Fig. 8 shows a close-up of the middle plot in Fig. 8. This specific signal $x_s(t)$ is of high frequency compared to the dynamics of the microrobot in vertical flight, and therefore information rich, which implies that this sequence is a good choice of dataset for estimating the mapping Ψ, using modern identification techniques.

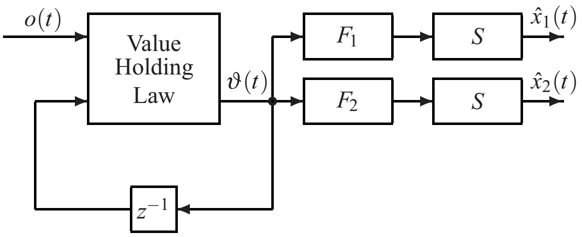

Fig. 9. Block diagram of the two methods proposed for mapping the optical-flow signal, $o(t)$, to the estimated altitude, $\hat{x}(t)$, i.e., finding an operator Ψ so that $\hat{x}(t) = [\Psi o](t)$. The filter F_1 is estimated using the $n4sid$ subspace system identification method [27]. The filter F_2 is a simple discrete-time integrator. The operator S saturates the signal so that the estimate $\hat{x}(t)$ remains inside a desired range. The subindices of $\hat{x}_1$ and $\hat{x}_2$ indicates which of the two linear filters has been employed in the estimation.

Two simple methods are proposed for representing Ψ, which are illustrated in Fig. 9. The first method uses the LTI filter F_1 and yields $\hat{x}_1(t)$; the second method uses the LTI filter F_2 and yields $\hat{x}_2(t)$. There are not other differences between the two mapping methods. The value holding law is defined as

$$\vartheta(t) = \begin{cases} \vartheta(t-1) & \text{if } o(t) = 0 \\ o(t) & \text{otherwise,} \end{cases} \tag{6}$$

where $\vartheta(t)$ is the input to the LTI filters $F_1(z)$ and $F_2(z)$, as shown in Fig. 9. Here, $F_1(z)$ is identified with the subspace state-space $n4sid$ algorithm in MATLAB [27], using the data in Fig. 8, assuming that ϑ is the input and $x_s(t)$ is the output to the filter to be identified. The identification algorithm yields a 48th-order discrete-time state-space realization, which is reduced to a second-order representation, using balanced reduction techniques [28], [29]. The resulting approximated state-space representation matrices are

$$A_{F_1} = \begin{bmatrix} 0.99999 & 0.00007 \\ 0.00007 & -0.73670 \end{bmatrix}, \quad B_{F_1} = \begin{bmatrix} -0.00092 \\ 0.00590 \end{bmatrix},$$
$$C_{F_1} = [-0.00001 \quad 0.00007], \quad D_{F_1} = 0.00000.$$

The filter $F_2(z)$ is simply a discrete-time integrator with the form

$$F_2(z) = K_I \frac{z+1}{z-1}, \tag{7}$$

where K_I is identified by formulating and solving a simple least squares problem. In this particular case, the identified parameter is $K_I = 1.47404 \times 10^{-4}$. The idea of using an integrator comes from noting that the spikes in $o(t)$ are proportional to velocity.

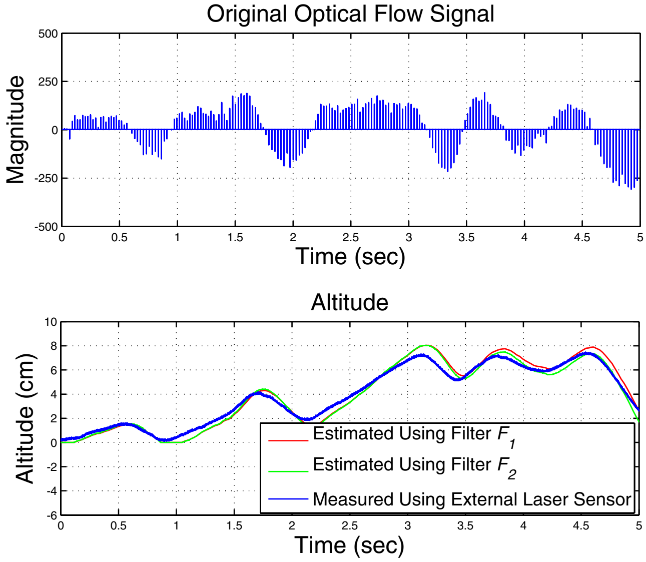

Fig. 10. Example showing the use of the two proposed methods in Fig. 9 for mapping the optical-flow signal, $o(t)$, to the estimated altitude, $\hat{x}(t)$. *Upper Plot:* Original optical-flow signal. *Bottom Plot:* Altitude estimated using filter F_1 (red), altitude estimated using filter F_2 (green), and altitude measured using the external laser displacement sensor in Figs. 2 and 3 (blue).

Additionally, the low-pass shape of $F_1(z)$ indicates that many tuned low-pass filters might be suitable for the task considered here. The last element that needs description in Fig. 9 is the operator S, which is a saturation law with the form

$$\hat{x}(t) = \begin{cases} \hat{x}_{\min} & \text{if } [F\vartheta](t) \leqslant \hat{x}_{\min} \\ \hat{x}_{\max} & \text{if } [F\vartheta](t) \geqslant \hat{x}_{\max} \\ [F\vartheta](t) & \text{otherwise.} \end{cases} \tag{8}$$

An example illustrating the use of both methods is shown in Fig. 10. According to several trials, it was found that the use of F_1 yields slightly better results than the use of F_2. For this reason, the flight experiments presented in Subsection IV-B are performed using F_1 to compute $\hat{x}(t)$ from the optical-flow signal $o(t)$.

As shown in Subsection IV-B, the method described earlier works satisfactorily under the experimental conditions considered here, but it is important to note that there are some potential limitations. Given that the model relating optical flow and altitude is identified using a visual pattern at a fixed depth from the sensor, and that the optical-flow signal is inversely proportional to the distance from the visual pattern [30], the estimated altitude will correspond to the true altitude only when the visual pattern used during the identification process remains at the same fixed distance from the sensor's lens. If this distance is changed, the altitude estimate will scale inversely proportional to the distance change. Here, we consider visual patterns at a fixed distance from the sensor, because this allows us to consistently compare the optical-flow-based estimate of the robot's altitude with the true altitude measured using the external laser position sensor in Figs. 2 and 3, used as a benchmark. This approach is sufficient for tackling the 1-DOF experimental cases described in Section II and detailed in Subsection IV-B. Once new robotic prototypes capable of unconstrained free flight are developed, more sophisticated 3-DOF algorithms will be developed, taking into account depth among other relevant variables.

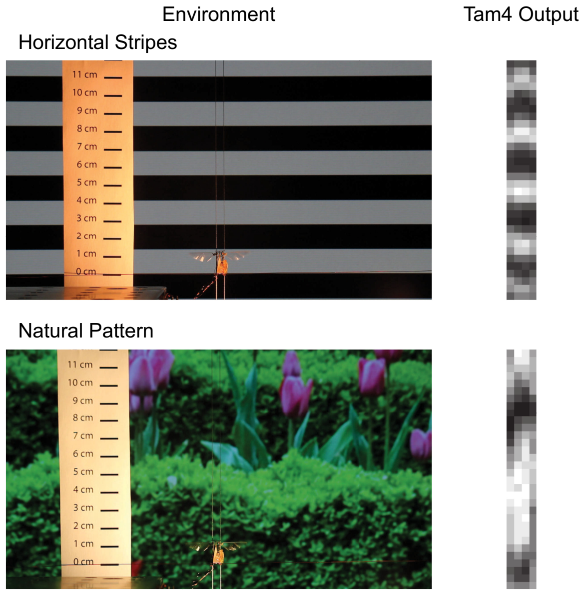

Fig. 11. *Upper Images:* Photograph of horizontally striped pattern (left) with the respective Tam4 image sensor response (right). *Bottom Images:* Photograph of natural-looking pattern (left) with the respective Tam4 image sensor response (right). Compared to the horizontally striped pattern, the natural-looking pattern is non-homogeneous. Sensor response is resized and scaled in intensity to $[0, 255]$ for visualization purposes only.

B. *Flight Experiments*

In this subsection, we consider two kinds of visual patterns for generating optical flow: a textured screen and a natural-looking image, both shown in Fig. 11. To demonstrate the capabilities of the sensing system and the method used for generating and processing optical flow, we present six experimental cases in which the optical-flow-based sensor described in Section III is used for controlling the altitude of the microrobot in Fig. 1. The results corresponding to Case 1 are summarized in Figs. 12 and 14. In this case, the objective is to make the microrobot reach the desired vertical position of 4.5 cm and hover at that position until *Time* $= 15$ s, while the vertical position is estimated by processing a static textured background image consisting of black and white horizontal stripes. The textured pattern and its corresponding Tam4 image sensor response are shown in the upper section of Fig. 11 (also see Fig. 14). The upper plot of Fig. 12 compares the reference $x_d(t)$, the true altitude $x(t)$, measured using the external laser position sensor depicted in Fig. 2, and the optical-flow-based measurement $\hat{x}(t)$ in black, blue, and red, respectively. The middle and bottom plots in Fig. 12 show the control signal $u(t)$ and a close-up of the middle plot, respectively. As can be seen in the middle plot of Fig. 12, the robot starts flapping at *Time* $= 1$ s, with a fixed amplitude of $a_u(t) = \frac{1}{3}$. Then, at *Time* $= 5$ s, the control loop is closed and the control signal $a_u(t)$ immediately reaches its upper bound $\overline{a_u} = \frac{14}{15}$ and stays at that value until the *RoboBee* reaches the desired altitude of 4.5 cm. While the robot hovers at 4.5 cm, the

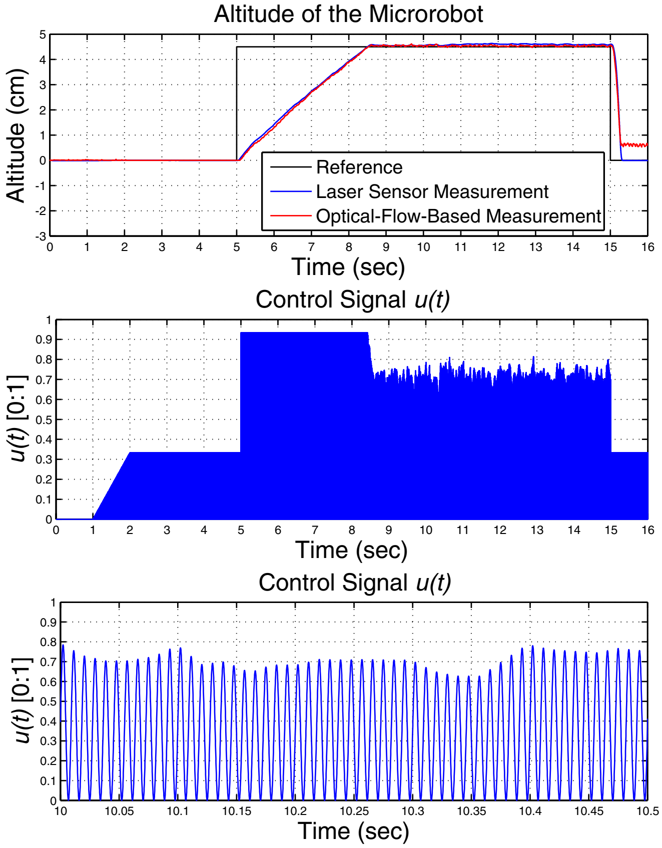

Fig. 12. Hovering with static background (Experimental Case 1). *Upper Plot:* Reference $x_d(t)$, optical-flow-based altitude measurement $\hat{x}(t)$, altitude measured with the external laser position sensor, $x(t)$ (true value). *Middle Plot:* Control signal $u(t) = a_u(t)\sin(2\pi f_u t)$, with $\underline{a_u} = \frac{1}{3}$, $\overline{a_u} = \frac{14}{15}$, and $f_u = 110$ Hz. *Bottom Plot:* Close-up of the control signal $u(t)$.

controller compensates for disturbances by varying the value of $a_u(t)$, as shown in the middle plot of Fig. 12. Frames from a video sequence of the experiment are shown in Fig. 14.

Case 2 is summarized in Figs. 13-(a) and 15. In this case, the objective is to make the microrobot reach the desired vertical position of 4.5 cm and then track a sinusoidal trajectory with amplitude 1 cm and frequency 0.1 Hz, while the vertical position is estimated by processing a static textured background image consisting of black and white horizontal stripes (see Figs. 11 and 15). Fig. 13-(a) compares the reference $x_d(t)$, the true altitude $x(t)$, measured using the external laser position sensor depicted in Fig. 2, and the optical-flow-based measurement $\hat{x}(t)$ in black, blue, and red, respectively. The plot of the control signal $u(t)$ is omitted for the sake of brevity. A complete set of plots for Cases 2 through 6 is shown in the supplemental pdf file in [31].

In Cases 1 and 2, the controller performance is excellent and the control error is small (almost zero). However, it is important to state that in Case 2 a slow, almost imperceptible, downward drift affects the vertical position of the microrobot. This small discrepancy between $x(t)$ and $\hat{x}(t)$ can be explained by the existence of sensing noise, which accumulates over time due to the integration of $\vartheta(t)$, when $\hat{x}(t)$ is computed according to the method in Fig. 9. Note that the quality of the altitude control experimental results presented here is comparable to the quality of the results in [4], obtained with the use of the external bulky laser position sensor depicted in Fig. 2. This is compelling evidence that on-board optical-flow-based sensors can be used for controlling position and velocity of *RoboBees*, by processing static background images.

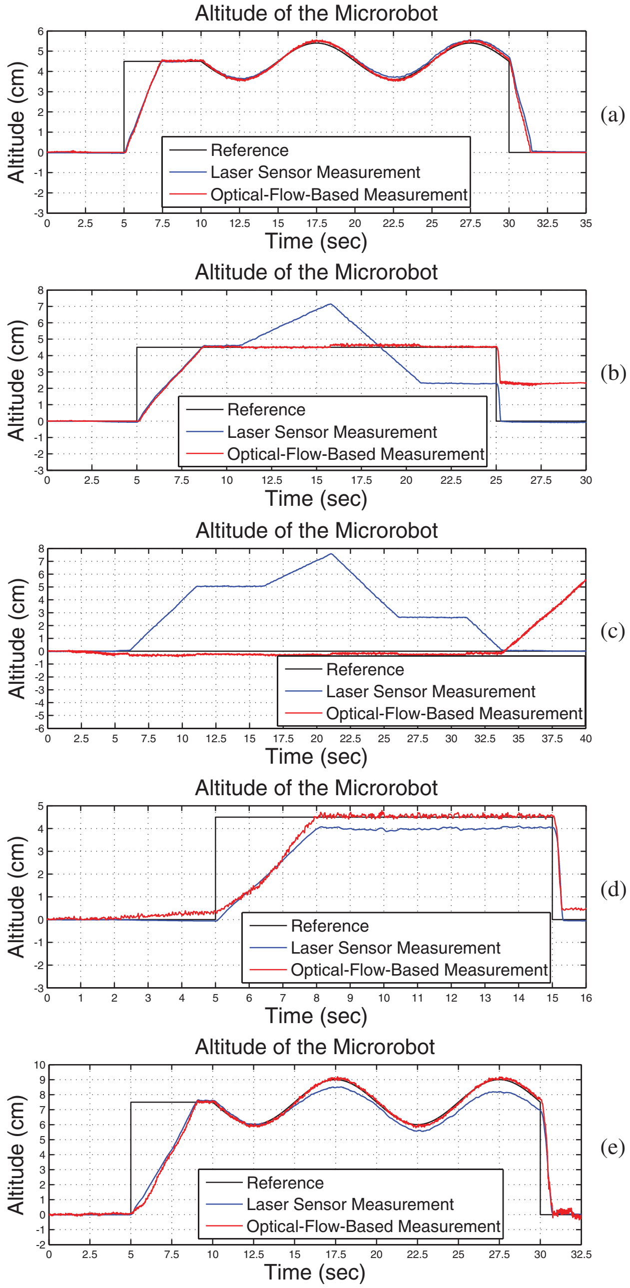

Fig. 13. Comparison of the reference $x_d(t)$, optical-flow-based altitude measurement $\hat{x}(t)$, and altitude measured with the external laser position sensor, $x(t)$ (true value). (a) Experimental Case 2, demonstrating trajectory following with static background. (b) Experimental Case 3, demonstrating motion tracking. (c) Experimental Case 4, demonstrating motion tracking with reference $x_d(t) = 0$. (d) Experimental Case 5, demonstrating hovering with natural-looking pattern. (e) Experimental Case 6, demonstrating, trajectory following with natural-looking pattern. A complete set of plots showing the control signals for each case is shown in [31].

The results corresponding to Case 3 are shown in Figs. 13-(b) and 16. In this case, the robot is required to reach the vertical

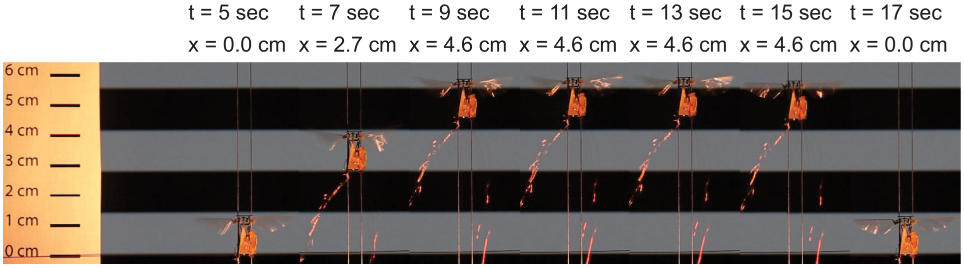

Fig. 14. Video sequence showing experimental Case 1. The *true* vertical position of the microrobot, $x(t)$, is measured using an external laser position sensor. The controller uses the optical-flow-based altitude measurement, $\hat{x}(t)$. A movie of the entire experiment is shown in the supplemental movie S1 in [32].

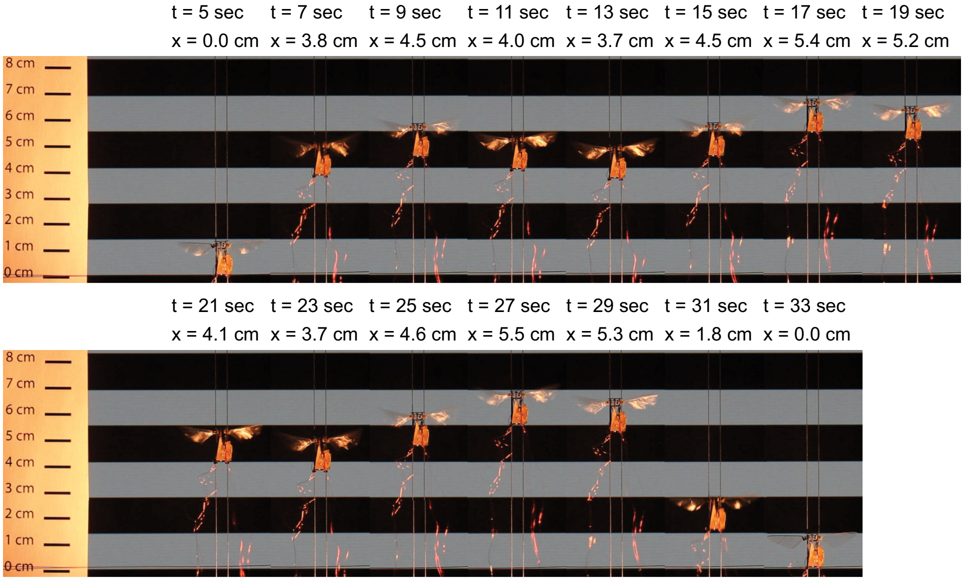

Fig. 15. Video sequence showing experimental Case 2. The *true* vertical position of the microrobot, $x(t)$, is measured using an external laser position sensor. The controller uses the optical-flow-based altitude measurement, $\hat{x}(t)$. A movie of the entire experiment is shown in the supplemental movie S1 in [32].

position of 4.5 cm, hover there for some seconds and then track a moving image. The moving image is the entire patterned screen, which moves upward at $\frac{1}{2}$ cm/s for 5 s and then moves downward at a higher speed of 1 cm/s for another 5 s before stopping until the experimental test is finished at *Time* $= 25$ s. Fig. 13-(b) compares the reference $x_d(t)$, the estimated altitude $\hat{x}(t)$, and the true vertical position $x(t)$. Once the robot reaches an altitude of 4.5 cm, the reference is fixed until the controller is turned off at *Time* $= 25$ s. The estimated altitude $\hat{x}(t)$ is computed from the optical flow generated by capturing an image of the textured screen positioned in front of the optical sensor. Therefore, any movement of the textured screen is seen by the controller as a disturbance that needs to be rejected. In order to minimize the control error, the robot follows the patterned screen upward and downward. In this situation, the control system is no longer capable of maintaining a specified desired altitude relative to the ground, but is successful at maintaining a desired position relative to the screen. This tells us that when optical flow is used, navigation should be accomplish by controlling speed and not position. Fortunately, the results presented in this paper suggest that if the correct mapping from optical flow to velocity was to be found, similar control laws to the one proposed in Section III could be applied to the control of velocity. Note that from a control perspective, hovering and motion tracking are equivalent, because in both cases the robot remains still and rejects disturbances relative to a set point in the texture of the screen. This is clear from the shape of the signal $\hat{x}(t)$ in Fig. 13-(b). In order to see this point, consider the description of the system

$$x(t) = [Ga_u](t) + \nu_1(t), \tag{9}$$

$$\hat{x}(t) = [Ga_u](t) + \nu_1(t) + \nu_2(t), \tag{10}$$

where ν_1 is the true disturbance affecting the system, ν_2 is the artificial disturbance introduced by the movement of the patterned screen, x is the true altitude of the robot, and $\hat{x}$ is the noise-free optical-flow-based estimate of the robot's altitude. The output sensitivity function, S_o, associated with the proposed controller maps $\nu_1 + \nu_2$ to $\hat{x}$ as

$$\hat{x} = S_o\left(\nu_1 + \nu_2\right). \tag{11}$$

From [4], it is clear that S_o is a high-pass filter, and therefore, the signal $\nu_1 + \nu_2$ is rejected if the frequency content of it is below the cutoff frequency of S_o. Thus, the control objective is to reject $\nu_1 + \nu_2$, which means that for small values of ν_1, the robot will follow the reference $-\nu_2$.

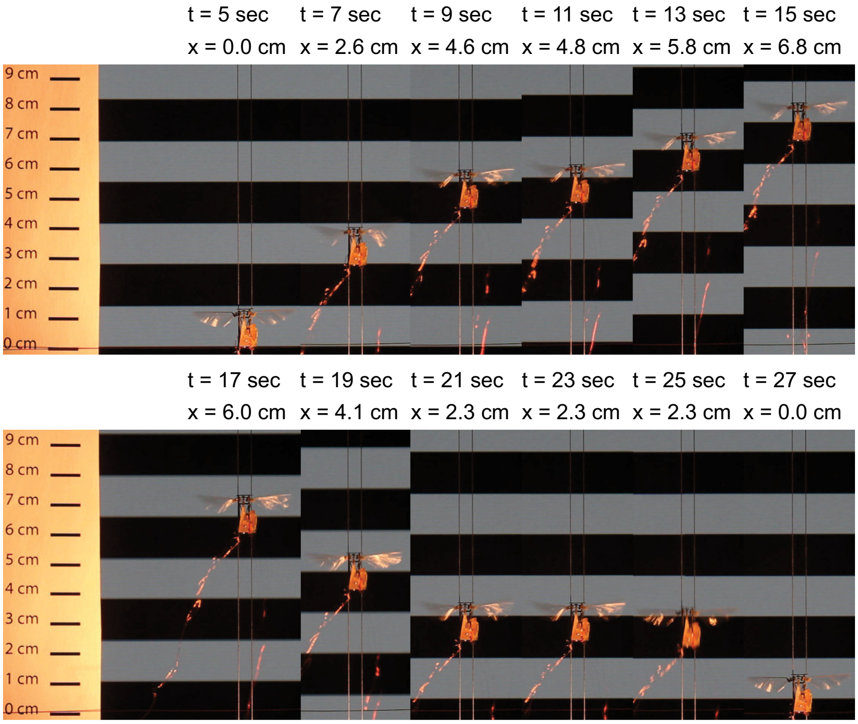

Fig. 16. Video sequence showing experimental Case 3. The *true* vertical position of the microrobot, $x(t)$, is measured using an external laser position sensor. The controller uses the optical-flow-based altitude measurement, $\hat{x}(t)$. A movie of the entire experiment is shown in the supplemental movie S1 in [32].

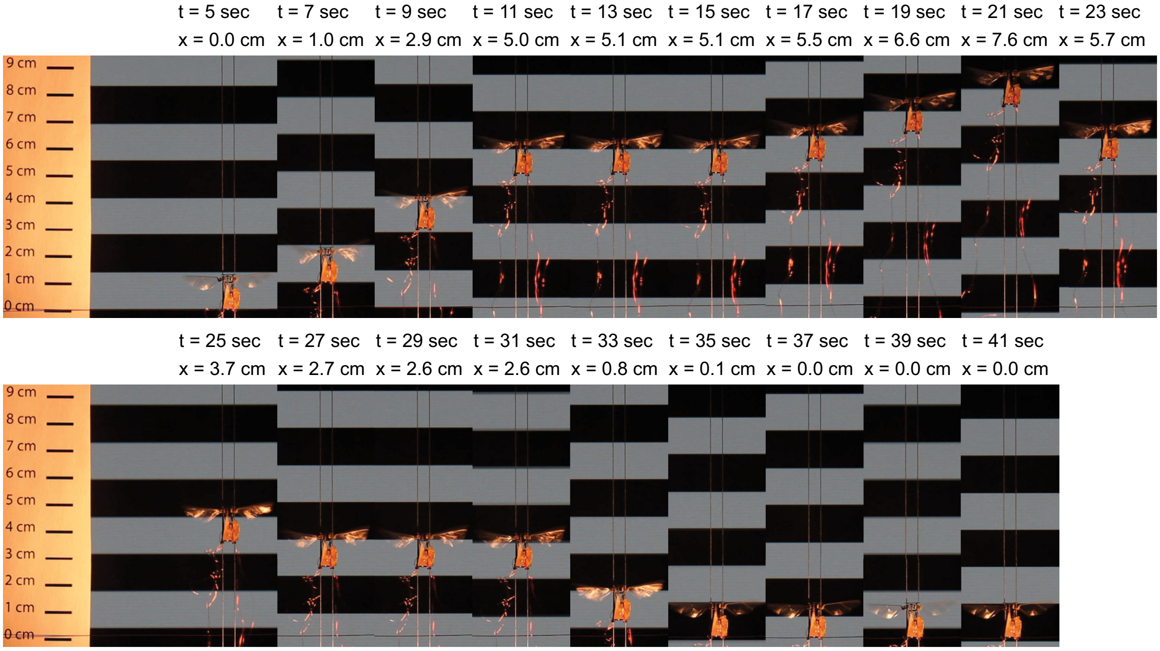

Fig. 17. Video sequence showing experimental Case 4. The *true* vertical position of the microrobot, $x(t)$, is measured using an external laser position sensor. The controller uses the optical-flow-based altitude measurement, $\hat{x}(t)$. A movie of the entire experiment is shown in the supplemental movie S1 in [32].

Case 4, shown in Fig. 13-(c) is a generalization of Case 3, in which the microrobot takes off and lands tracking the patterned screen. In this case, the reference $x_d(t)$ is set to zero, and therefore, any movement of the screen is seen by the controller as a disturbance that needs to be rejected in order to maintain an estimated position $\hat{x}(t) = 0$. The true trajectory $x(t)$ followed by the robot is shown in blue in Fig. 13-(c). Using Fig. 13-(c), the controller performance can be assessed by comparing $\hat{x}(t)$, in red, with the reference $x_d(t)$, in black. More noticeable, the high performance achieved with the use of the proposed controller can be assessed from the video sequence in Fig. 17 and the supporting movie S1.mp4 in [32].

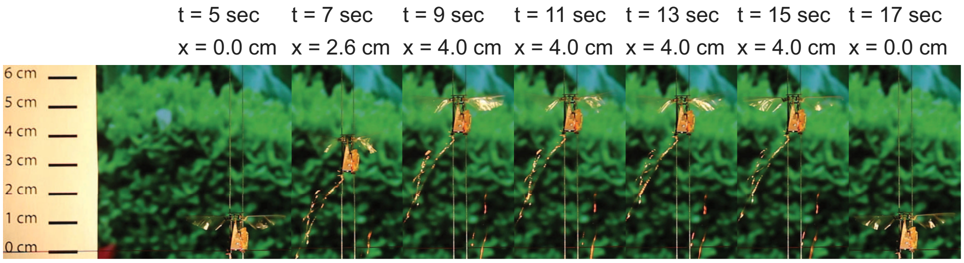

Fig. 18. Video sequence showing experimental Case 5. The *true* vertical position of the microrobot, $x(t)$, is measured using an external laser position sensor. The controller uses the optical-flow-based altitude measurement, $\hat{x}(t)$. A movie of the entire experiment is shown in the supplemental movie S1 in [32].

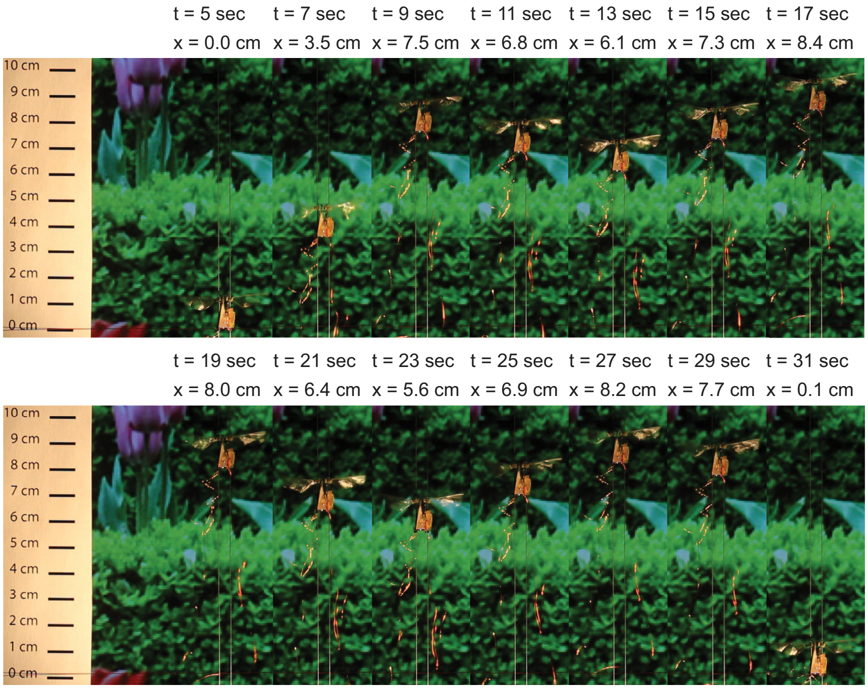

Fig. 19. Video sequence showing experimental Case 6. The *true* vertical position of the microrobot, $x(t)$, is measured using an external laser position sensor. The controller uses the optical-flow-based altitude measurement, $\hat{x}(t)$. A movie of the entire experiment is shown in the supplemental movie S1 in [32].

The time series associated with Case 5 is shown in Fig. 13-(d). This case demonstrates hovering using optical flow that is obtained by processing a natural-looking pattern consisting of plants and flowers. In this case, the objective is to make the microrobot reach the desired vertical position of 4.5 cm and hover at that position until $Time = 15$ s. The difference between this case and Case 1 is that the vertical position is estimated by processing a background image that is not a perfectly symmetric textured pattern formed by black and white horizontal stripes. The pattern use in Case 5 and its corresponding Tam4 image sensor response are shown in the bottom section of Fig. 11 (also see Fig. 18). Fig. 13-(d) shows that the control of velocity is almost perfect, since the robot hovers at a constant altitude throughout the experiment, but that there exists a significant disagreement between the optical-flow-based estimated altitude and the true altitude measured using the external laser position sensor illustrated in Fig. 2 and shown in Fig. 3. This suggests that, in this particular case, the corresponding mapping from optical flow to altitude is nonlinear and cannot be correctly identified with the use of the linear identification methods described in the previous section. Another plausible explanation is that a nonuniform pattern increases the noise in the optical-flow signal. Regardless of the cause of the issue, note that combining the control law in (4) and a mapping with the same structure of the system in Fig. 9, speed can be controlled. A video sequence of the experimental Case 5 is shown in Fig. 18. Also, see the supporting movie S1.mp4 in [32].

Finally, Case 6, shown in Figs. 13-(e) and 19, is a trajectory following experiment, similar to the experiment in Case 2, but performed using the natural-looking pattern on the bottom of Fig. 11. From Fig. 13-(e), the control performance can be assessed by comparing $\hat{x}(t)$, in red, with the reference $x_d(t)$, in black. The good agreement between both signals is evidence of high performance control. The quality of the optical-flow-based position estimate $\hat{x}(t)$, in red, as compared to the true position $x(t)$, in blue, is excellent during the initial tracking of the sinusoidal reference. However, the estimate $\hat{x}(t)$ slowly diverges from the true position $x(t)$ over time. This case also suggests the need for a control strategy based on velocity rather than position.

V. CONCLUSION

In this paper, we presented experimental results on the controlled vertical flight of a 101-mg flapping-wing microrobot, in which for the first time altitude was measured using an on-board optical-flow-based sensor. During the development of this research, many challenges were overcome, including the fabrication and integration of on-board sensing capabilities into the microrobot, while meeting the strict mass and size requirements for liftoff. Also, this paper described the design and implementation of real-time controllers and signal processing algorithms required for the fusion of on-board sensing with the microrobot. The achieved control performance with the on-board sensor is comparable to the one in [4], where an external laser displacement sensor was used to measure altitude. The research presented in this paper is a key step toward achieving the goal of complete autonomy for at-scale flapping-wing microrobots.

REFERENCES

[1] N. O. Pérez-Arancibia, J. P. Whitney, and R. J. Wood, "Lift force control of a flapping-wing microrobot," in *Proc. Amer. Control Conf.*, San Francisco, CA, Jul. 2011, pp. 4761–4768.

[2] N. O. Pérez-Arancibia, J. P. Whitney, and R. J. Wood, "Lift force control of flapping-wing microrobots using adaptive feedforward schemes," *IEEE/ASME Trans. Mechatronics*, vol. 18, no. 1, pp. 155–168, Feb. 2013.

[3] R. J. Wood, "The first takeoff of a biologically inspired at-scale robotic insect," *IEEE Trans. Robot.*, vol. 24, no. 2, pp. 341–347, Apr. 2008.

[4] N. O. Pérez-Arancibia, K. Y. Ma, K. C. Galloway, J. D. Greenberg, and R. J. Wood, "First controlled vertical flight of a biologically inspired microrobot," *Bioinspir. Biomim.*, vol. 6, no. 3, pp. 036009-1–036009-11, Sep. 2011.

[5] W. E. Green, P. Y. Oh, and G. Barrows, "Flying insect inspired vision for autonomous aerial robot maneuvers in near-earth enviroments," in *Proc. Int. Conf. Robot. Autom.*, New Orleans, LA, Apr. 2004, pp. 2347–2352.

[6] R. Dudley, *The Biomechanics of Insect Flight*. Princeton, NJ: Princeton Univ. Press, 2000.

[7] D. Burkhardt, "On the vision of insects," *J. Comput. Physiol. A*, vol. 120, no. 1, pp. 33–50, Jan. 1977.

[8] M. V. Srinivasan, S. W. Zhang, J. S. Chahl, G. Stange, and M. Garratt, "An overview of insect-inspired guidance for application in ground and airborne platforms," in *Proc. Inst. Mech. Eng., J. Aerosp. Eng.*, Jun. 2004, vol. 218, no. 6, pp. 375–388.

[9] G. L. Barrows, "Mixed-mode VLSI optic flow sensors for micro air vehicles," Ph.D. dissertation, Univ. Maryland, College Park, MD, 1999.

[10] G. L. Barrows, K. T. Miller, and B. Krantz, "Fusing neuromorphic motion detector outputs for robust optic flow measurement," in *Proc. Int. Joint Conf. Neural Netw.*, Washington, DC, Jul. 1999, pp. 2296–2301.

[11] G. L. Barrows and C. Neely, "Mixed-mode VLSI optic flow sensors for in-flight control of a micro air vehicle," in *Proc. SPIE*, vol. 4109, pp. 52–63, Nov. 2000.

[12] G. L. Barrows, J. S. Chahl, and M. V. Srinivasan, "Biomimetic inspired visual sensing and flight control," *Aeronaut. J.*, vol. 107, no. 1069, pp. 159–168, Mar. 2003.

[13] F. Ruffier, S. Viollet, S. Amic, and N. Franceschini, "Bio-inspired optical flow circuits for the visual guidance of micro-air vehicles," in *Proc. IEEE Int. Symp. Circuits Syst.*, Bangkok, Thailand, May 2003, pp. 846–849.

[14] W.-C. Wu, L. Schenato, R. J. Wood, and R. S. Fearing, "Biomimetic sensor suite for flight control of a micromechanical flying insect: Design and experimental results," in *Proc. IEEE Int. Conf. Robot. Autom.*, Taipei, Taiwan, R.O.C., Sep. 2003, pp. 1146–1151.

[15] F. Ruffier and N. Franceschini, "Optic flow regulation: The key to aircraft automatic guidance," *Robot. Autom. Syst.*, vol. 50, no. 4, pp. 177–194, Mar. 2005.

[16] R. J. Wood, S. Avadhanula, E. Steltz, M. Seeman, J. Entwistle, A. Bachrach, G. Barrows, S. Sanders, and R. S. Fearing, "An autonomous palm-sized gliding micro air vehicle," *IEEE Robot. Autom. Mag.*, vol. 14, no. 2, pp. 82–91, Jun. 2007.

[17] J.-C. Zufferey, A. Klaptocz, A. Beyeler, J.-D. Nicoud, and D. Floreano, "A 10-gram vision-based flying robot," *Proc. Inst. Mech. Eng., J. Aerosp. Eng.*, vol. 21, no. 14, pp. 1671–1684, Dec. 2007.

[18] F. Garcia Bermudez and R. Fearing, "Optical flow on a flapping wing robot," in *Proc. IEEE/RSJ Int. Conf. Intell. Robot. Syst.*, St. Louis, MO, Oct. 2009, pp. 5027–5032.

[19] R. J. Wood, E. Steltz, and R. S. Fearing, "Nonlinear performance limits for high energy density piezoelectric bending actuators," in *Proc. IEEE Int. Conf. Robot. Autom.*, Barcelona, Spain, Apr. 2005, pp. 3633–3640.

[20] J. P. Whitney and R. J. Wood, "Aeromechanics of passive rotation in flapping flight," *J. Fluid Mech.*, vol. 660, pp. 197–220, Oct. 2010.

[21] F.-O. Lehmann and M. H. Dickinson, "The control of wing kinematics and flight forces in fruit flies (Drosophila spp.)," *J. Exp. Biol.*, vol. 201, no. 3, pp. 385–401, Feb. 1998.

[22] C. P. Ellington, "The aerodynamics of hovering insect flight. vi. lift and power requirements," *Phil. Trans. R. Soc. Lond. B*, vol. 305, no. 1122, pp. 145–185, Feb. 1984.

[23] T. Weis-Fogh, "Quick estimates of flight fitness in hovering animals, including novel mechanisms for lift production," *J. Exp. Biol.*, vol. 59, no. 1, pp. 169–230, Aug. 1973.

[24] G. Barrows, "Low profile camera and vision sensor," U.S. Patent 2011/0026141 A1, Feb. 3, 2011.

[25] A. Klaptocz, *Miniature Cameras for Ultra-Light Flying Robots*, E&CE 4th Year Design Project, Univ. Waterloo and Ecole Polytechnique Fédérale de Lausanne, Lausanne, Switzerland, 2005.

[26] M. V. Srinivasan, "An image-interpolation technique for the computation of optic flow and egomotion," *Biol. Cybern.*, vol. 71, no. 5, pp. 401–415, Sep. 1994.

[27] P. Van Overschee and B. De Moor, *Subspace Identification for Linear Systems*. Boston, MA: Kluwer, 1996.

[28] A. J. Laub, M. T. Heath, C. C. Paige, and R. C. Ward, "Computation of system balancing transformations and other applications of simultaneous diagonalization algorithms," *IEEE Trans. Autom. Control*, vol. 32, no. 2, pp. 115–122, Feb. 1987.

[29] G. E. Dullerud and F. Paganini, *A Course in Robust Control Theory*. New York: Springer-Verlag, 2000.

[30] J. J. Koenderink and A. J. van Doorn, "Facts on optic flow," *Biol. Cybern.*, vol. 56, no. 4, pp. 247–254, Jun. 1987.

[31] N. O. Pérez-Arancibia, P.-E. J. Duhamel, G. L. Barrows, and R. J. Wood. (2011, Oct.). *S2* [Online]. Available:http://micro.seas.harvard.edu/TMech2011OptFlow/S2.pdf

[32] P.-E. J. Duhamel, N. O. Pérez-Arancibia, G. L. Barrows, and R. J. Wood. (2011, Oct.). *S1* [Online]. Available:http://micro.seas.harvard.edu/TMech2011OptFlow/S1.mp4

Pierre-Emile J. Duhamel (S'11) received the A.B. degree in computer science, and chemistry and physics from Harvard University, Cambridge, MA, in 2009, where he is currently working toward the Ph.D. degree in computer science at the School of Engineering and Applied Sciences. His research interests include computer vision, computer hardware, and robotics. Mr. Duhamel received a National Science Foundation Graduate Research Fellowship in 2010.

Néstor O. Pérez-Arancibia (S'05–M'08) received the Ph.D. degree from the Department of Mechanical and Aerospace Engineering, University of California, Los Angeles (UCLA), in 2007. From October 2007 to March 2010, he was a Postdoctoral Scholar in the Laser Beam Control Laboratory and also with the Mechatronics and Controls Laboratory in the Department of Mechanical and Aerospace Engineering, UCLA. Since April 2010, he has been a Postdoctoral Fellow in the Microrobotics Laboratory and the Wyss Institute for Biologically Inspired Engineering, Harvard University, Cambridge, MA. His current research interests include microrobotics, feedback control, adaptive filtering, adaptive optics, and mechatronics.

Geoffrey L. Barrows received the B.S. degree in applied mathematics from the University of Virginia, Charlottesville, in 1993, the M.S. degree in electrical engineering from Stanford University, Stanford, CA, in 1994, and the Ph.D. degree in electrical engineering from the University of Maryland, College Park, in 1999. He is the Founder and President of Centeye, Inc., Washington, DC, a company that makes image sensor chips and compact vision sensors for robotics and embedded vision. Prior to Centeye, he was with the Naval Research Laboratory while completing his graduate studies. Dr. Barrows was named to the *MIT Technology Review*'s TR-100 list in 2003.

Robert J. Wood (M'01) received the Master's and Ph.D. degrees from the Department of Electrical Engineering and Computer Sciences, University of California, Berkeley, in 2001 and 2004, respectively. He is currently the Charles River Professor of Engineering and Applied Sciences in the School of Engineering and Applied Sciences and the Wyss Institute for Biologically Inspired Engineering at Harvard University, Cambridge, MA. His research interests include microrobotics and bioinspired robotics.